Journal of Solid State Chemistry 185 (2012) 172–179

Contents lists available at SciVerse ScienceDirect

Journal of Solid State Chemistry

journal homepage: www.elsevier.com/locate/jssc

Controlled synthesis of $MnSn(OH)_6$/graphene nanocomposites and their electrochemical properties as capacitive materials

Gongkai Wang [a,b], Xiang Sun [b], Fengyuan Lu [b], Qingkai Yu [c], Changsheng Liu [a], Jie Lian [b,*]

[a] Key Laboratory for Anisotropy and Texture of Materials of Ministry of Education, Northeastern University, Shenyang, Liaoning 110004, China
[b] Department of Mechanical, Aerospace & Nuclear Engineering, Rensselaer Polytechnic Institute, Troy, NY 12180, USA
[c] Department of Electrical Engineering, Texas State University, San Marcos, TX 78666, USA

ARTICLE INFO

Article history:
Received 23 July 2011
Received in revised form
25 October 2011
Accepted 6 November 2011
Available online 15 November 2011

Keywords:
Graphene
Binary metal
Nanocomposites
Capacitive

ABSTRACT

We report the synthesis of novel $MnSn(OH)_6$/graphene nanocomposites produced by a co-precipitation method and their potential application for electrochemical energy storage. The hydroxide decorated graphene nanocomposites display better performance over pure $MnSn(OH)_6$ nanoparticles because the graphene sheets act as conductive bridges improving the ionic and electronic transport. The crystallinity of $MnSn(OH)_6$ nanoparticles deposited on the surface of graphene sheets also impacts the capacitive properties as electrodes. The maximum capacitance of 31.2 F/g (59.4 F/g based on the mass of $MnSn(OH)_6$ nanoparticles) was achieved for the sample with a low degree of crystallinity. No significant degradation of capacitance occurred after 500 cycles at a current density of 1.5 A/g in 1 M Na_2SO_4 aqueous solution, indicating an excellent electrochemical stability. The results serve as an example demonstrating the potential of integrating highly conductive graphene networks into binary metal hydroxide in improving the performance of active electrode materials for electrochemical energy storage applications.

1. Introduction

Electrochemical energy storage devices based on supercapacitors are classified as electrochemical double layer capacitors (EDLCs) and pseudo-capacitors depending on the specific energy storage mechanisms of ion-adsorption and fast redox reactions, respectively. EDLCs exhibit an excellent cycle life, and typically carbon materials with high surface area are used as electrodes; while the energy storage capability is limited for carbon-based EDLCs [1]. Pseudo-capacitive materials such as hydroxides [2], oxides [3] and conductive polymers [4] display greater specific capacitance than that of carbon materials, but are limited by the poor electrical conductivity, low power density and instability induced degradations during cycling [5–8]. Progresses were achieved so far to couple pseudo-capacitive materials with carbon materials together for maximizing performance in targeting high power and energy delivery capabilities [1,2,9,10]. Efforts have been conducted on incorporating pseudo-materials on different carbon networks including activated carbon, CNF [10], carbon monolith [11], template carbon [12] and CNT [13,14]. However, the intrinsic problems, such as poor electrical conductivity, improper building architecture and poor interaction between carbon and pseudo-capacitive materials, still limit their performance.

Graphene, a single-atomic-thick sheet, consists of sp^2-bonded carbon atoms in hexagonal lattice and possesses excellent physical and chemical properties. The two-dimensional geometry of graphene sheets is also ideal for fast ion transport and behaves as an excellent platform for integrating functional nano-sized pseudo-materials [15]. Previous studies have reported the synthesis of graphene based nanocomposites by various methods for supercapacitor applications. For example, $Ni(OH)_2$/graphene nanocomposites were synthesized by a hydrothermal method and specific capacitance of 1335 F/g in aqueous electrolyte at the current density of 2.8 A/g has been achieved [2]; MnO_2/graphene nanocomposites were fabricated using a soft chemical method coupled with microwave irradiation resulting in 310 F/g in aqueous electrolyte at the scan rate of 2 mV/s [16]; Polyaniline/graphene nanocomposites were synthesized by an *in situ* polymerization method and 1046 F/g at the scan rate of 1 mV/s was obtained in aqueous electrolyte [17].

Recently, binary metal oxides ($NiCo_2O_4$) as electrode materials for supercapacitors start to attract vast interests because of their excellent electrochemical properties such as gravimetric specific capacitance as high as 1400 F/g, long cycle stability, low costs and environmentally friendly performances [18]. It is expected that binary metal oxides may provide more redox reactions originated from both nickel and cobalt ions, as compared to the corresponding individual metal oxide.

In this paper, we demonstrated the synthesis of binary metal hydroxide $MnSn(OH)_6$/graphene nanocomposites and the integration

* Corresponding author. Fax: +1 5182766025.
E-mail address: LIANJ@rpi.edu (J. Lian).

0022-4596/$ - see front matter © 2011 Elsevier Inc. All rights reserved.
doi:10.1016/j.jssc.2011.11.015

of the conductive graphene nanosheets into the nanocomposites greatly improved the transport behavior and thus faradic efficiency, leading to the improved electrochemical performance. $MnSn(OH)_6$ belongs to a perovskite-structure type with the formula of $AB(OH)_6$ and can be synthesized by a simple, low cost and environmentally benign process [19]. The perovskite compound has been investigated in many areas including photocatalysts for benzene degradation, hydrogen storage [20,21] and in lithium-ion batteries [22–24]. However, limited efforts were focused on the perovskite compounds for supercapacitors application.

In this work, $MnSn(OH)_6$/graphene nanocomposites were synthesized by a simple co-precipitation method and their electrochemical performances have been explored. In this nanocomposites, graphene sheets play an important role, providing a large area conductive network, increasing the electrochemical activation, utilization and conductivity of $MnSn(OH)_6$ nanoparticles and also promoting the conductivity of the electrodes. In addition, the nano-sized $MnSn(OH)_6$ may offer more accessible diffusion pathways by inhibiting the agglomerations of graphene sheets, and decrease the interfacial transfer and diffusion resistance, contributing to the total specific capacitance. The effects of the crystallinity of $MnSn(OH)_6$ on electrochemical properties of the nanocomposites, as well as the microstructures were also discussed.

2. Experimental

2.1. Synthesis of graphene materials

2.1.1. Synthesis of graphite oxide

Graphite oxide (GO) was synthesized by the Hummers method [25]. Briefly, graphite powders (5 g, Sigma-Aldrich, cat# 282863, ~20 μm) were added to the mixture of concentrated H_2SO_4 (115 ml) and $NaNO_3$ (2.5 g) and stirred in an ice bath (0 °C). $KMnO_4$ (15 g) was added carefully to the solution, which was then maintained for 30 min at 35 °C followed by the addition of DI water (230 ml) slowly. The temperature of the reaction turned to 98 °C and the solution was kept for 15 min. After that additional DI water (355 ml) containing H_2O_2 (3 wt%, 5 ml) was added. The solid was obtained from centrifugation (3200 rpm, 5 min) followed by washing with excess DI water, 20 vol% HCl and ethanol, and the washing process was repeated three times. The final yellow brown GO powders were dried in vacuum at 40 °C for 12 h.

2.1.2. Synthesis of graphene sheets

Graphene sheets were produced by thermal exfoliation of as-synthesized GO powders. Generally, the GO (200 mg) was loaded in a crucible in a quartz tube under the argon protective environment. The quartz tube was quickly inserted into the heating zone of a tube furnace (GSL1100X, MTI, USA) which was preheated to 1050 °C and held there for 30 s. The GO can be exfoliated by rapid heating (2000 °C/min) into few layered graphene sheets [26].

2.2. Synthesis of $MnSn(OH)_6$/graphene nanocomposites

A schematic of the synthesis of $MnSn(OH)_6$/graphene nanocomposites is shown in Fig. 1. Typically, the as-synthesized graphene sheets (10 mg) were dispersed in DI water (100 ml) followed by sonication in an ultrasonic bath cleaner (EQ-VGT-1613QTD-110, 60 w, MTI, USA) to form a homogenous suspension, which was then transferred to a round-bottom flask. Meanwhile, an appropriate amount of $MnCl_2 \cdot 4H_2O$ was added into DI water (100 ml), and the solution was stirred at room temperature until $MnCl_2 \cdot 4H_2O$ was fully dissolved. Then the $MnCl_2 \cdot 4H_2O$ solution was added into the graphene suspension, and kept at desired reaction temperatures (0 °C, 25 °C, 50 °C and 80 °C) for 1 h. After that, 20 ml of $Na_2SnO_3 \cdot 3H_2O$ solution was poured into the above suspension according to the molar ratio of $MnCl_2 \cdot 4H_2O$ and $Na_2SnO_3 \cdot 3H_2O$ of 1:1. The mixed suspension was stirred at temperature of 0 °C, 25 °C, 50 °C and 80 °C for different reaction time (5 h, 15 h and 24 h). The solid was then collected by vacuum filtration through a PVDF membrane (Millipore membranes, GVWP04700, 0.22 μm pore size) and washed with DI water and ethanol several times to remove the residual ions in the products. The final samples were dried in air at 80 °C for 12 h. In order to investigate the effects of the crystallinity of $MnSn(OH)_6$ on electrochemical properties of the nanocomposites, a series of $MnSn(OH)_6$/graphene (30 wt%) samples were prepared under 0 °C, 25 °C, 50 °C and 80 °C for 5 h and under 80 °C for 5 h, 15 h and 24 h. For comparison, a pure $MnSn(OH)_6$ control sample, denoted as M, was also prepared followed the same procedure at room temperature for 24 h without the addition of the graphene sheets.

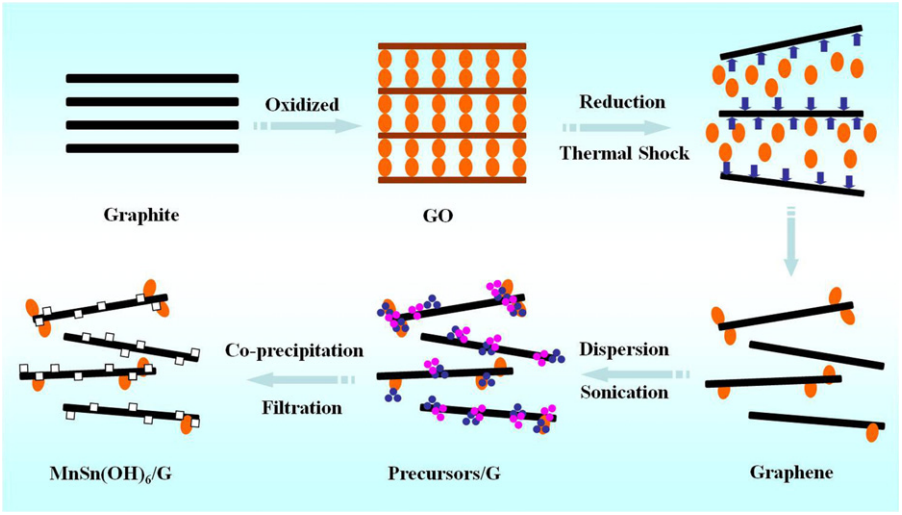

Fig. 1. Schematic of the synthesis of $MnSn(OH)_6$/graphene nanocomposites: Graphene oxide was synthesized by Hummers method; Graphene nanosheets were reduced by thermal exfoliation; Incorporation of metal hydroxide precursors attached on the reduced graphene nanosheets; Synthesis of final nanocomposites by co-precipitation and filtration methods.

2.3. Characterization

The X-ray diffraction (XRD) was performed on a PANanalytical X-ray diffraction system with a source wavelength of 1.542 Å at room temperature. The data collection time and scan step is 50 s/step and 0.02°, respectively. The X-ray photoelectron spectroscopy (XPS) was carried out on a PHI 5000 Versa Probe system, and the curve fitting was accomplished by MultiPak V 9.0 software. The morphology and microstructures of the samples were characterized by a field emission scanning electron microscopy (FESEM) (JSM-6335) and a JEOL 2010 transmission electron microscopy (TEM) operated with 200 KeV electron beam.

2.4. Preparation of electrodes and electrochemical measurements

The working electrode was prepared by mixing the electroactive materials, carbon black and polytetrafluoroethylene (PTFE) in mass ratio of 75:20:5 and dispersing in ethanol followed by sonication in an ultrasonic bath cleaner for 1 h. The suspension was dropped onto nickel foam (1×1 cm^2) and dried at 80 °C for 12 h. The foam with sample was compressed before test. The electrochemical properties of the samples were investigated under a standard three-electrode cell configuration using 1 M Na_2SO_4 aqueous solution as electrolyte at room temperature. Platinum wire and saturated calomel electrode (SCE) were used as counter electrode and reference electrode, respectively. Cyclic voltammograms (CV), galvanostatic charge/discharge and electrochemical impedance spectroscopy (EIS) were conducted on an electrochemical workstation (Ametek, Princeton Applied Research, Versa STAT 4). CV measurements were carried out between −0.5 and 0.5 V (vs. SCE) at various scan rates of 5, 10, 20 and 40 mV/s. Galvanostatic charge/discharge curves were tested in the potential range of −0.5–0.5 V (vs. SCE) at different current densities of 200, 300, 400 and 500 mA/g. EIS measurements were recorded in the frequency range from 0.1 Hz to 100 kHz at a 10 mV amplitude referring to the open circuit potential.

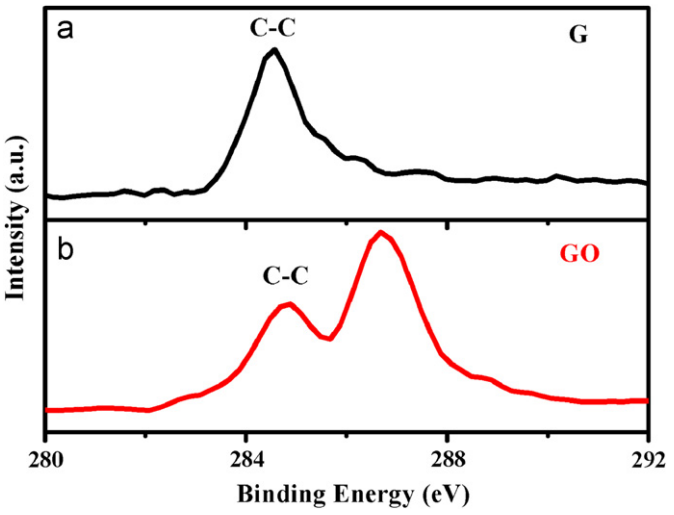

Fig. 2. C 1*s* XPS spectra of as-synthesized GO and the thermally exfoliated graphene.

3. Results and discussion

3.1. Microstructure characterizations

XPS was employed to evaluate the characteristic binding energy of C 1*s* peaks of GO and the thermally exfoliated graphene. As shown in Fig. 2(a), the C 1*s* spectra of GO revealed a large amount of oxygen-containing functional groups in the form of sp^3-hybridized saturated carbons including epoxy/hydroxyl (C–O, 286.2 eV), carbonyl (C═O, 287.8 eV) and carboxylate (O–C═O, 289.0 eV) [27]. In contrast, the peak intensity of oxygen-containing functionalities of the thermally shocked graphene decreased dramatically. The strong intensity of the C 1*s* peak of the thermally exfoliated graphene (Fig. 2(b)) was contributed mainly from the sp^2-hybridized graphitic carbons (C═C, 284.5 eV), suggesting most of oxygen-containing functionalities were removed during the thermal shock process. The C/O ratio was not used to determine the reduction level of the GO as it is difficult to obtain a fully dehydrated GO sample. Instead, the C 1*s* spectra was fitted by four components corresponding to functional groups at different carbon binding energies using the software MultiPak V 9.0 [28]. The relative area of the oxidized carbon and the sp^2 carbon for GO and G is 67.6% and 32.4%, 29.2% and 70.8%, respectively. The remaining functional groups attached on the surface or edge of graphene sheets may function as the nucleation sites for deposition of heteroatoms or molecules.

The crystallographic structures of the as-synthesized samples were confirmed by XRD (Fig. 3). The phase structure of the final production can be indexed to $MnSn(OH)_6$ (JCPDS 020-0727) with no impurities identified. In the Fig. 3(a), the major peak at the 2θ

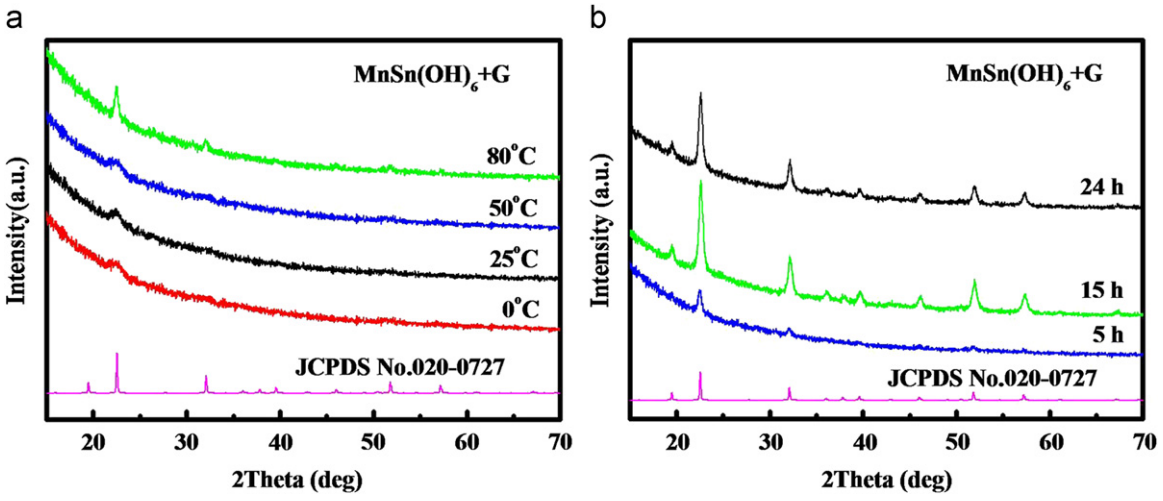

Fig. 3. XRD patterns of the $MnSn(OH)_6$/graphene samples synthesized under different temperatures and time: (a) synthesized under 0 °C, 25 °C, 50 °C and 80 °C for 5 h and (b) synthesized at 80 °C for 5 h, 15 h and 24 h.

around 22.6° (200) is broaden for the samples obtained at 0 °C, 25 and 50 °C for 5 h, corresponding to the poor crystallinity with very small size nanoparticle and significant amount of structural disordering or amorphous features. For the sample prepared at 80 °C for 5 h, the major peaks become sharper, indicating the improved crystallinity at a higher reaction temperature. Grain growth was observed with the increase of the reaction time, as shown in Fig. 3(b). The particle size of the sample obtained at 80 °C for 24 h was about 20 nm as calculated by the Scherrer Formula. Based on the above experimental results, it could be concluded that lower reaction temperature and shorter reaction time lead to poor crystalline compounds with a significant amount of amorphous nature.

The surface properties of the nanocomposites and the valence state of the elements were analyzed by XPS measurements (Fig. 4). Fig. 4(a) shows the large survey XPS spectra of the composite sample obtained at 80 °C for 24 h. Fig. 4(b) shows the C 1*s* XPS spectra of the graphene substrate with the peak centered at 284.5 eV, consistent with the previous XPS data of pure graphene sheets [27]. The Sn 3*d* XPS spectra shows peaks at 486.1 and 494.5 eV with a spin-energy separation of 8.41 eV (Fig. 4(c)), corresponding to the spin–orbit split Sn 3*d*5/2 and Sn 3*d*3/2 levels, respectively. The Mn 2*p* XPS spectra (Fig. 4(d)) shows two peaks centered at 641.1 and 652.8 eV with a spin–energy separation of 11.7 eV that can be assigned to Mn 2*p*3/2 and Mn 2*p*1/2. The peak positions of Sn and Mn presented in the corresponding XPS spectra illustrate that Sn and Mn are in the valence state of Sn (IV) and Mn (II), respectively [29,30].

The reaction time and temperature are two critical factors affecting the crystal structure, morphology and microstructure of the synthetic nanocomposites, which in turn may control their electrochemical behavior eventually. Three typical samples were selected with varied degrees of crystallinity from a significantly amorphous material, a well crystalline material and a material with a significant grain growth. These samples were obtained at 0 °C and 80 °C for 5 h and at 80 °C for 24 h, denoted as M+G−0−5 h, M+G−80−5 h and M+G−80−24 h, respectively. The TEM and SEM images (Fig. 5) show the morphology of these samples. The individual few layered graphene sheets display a highly wrinkled surface topology with a low contrast, consistent with the previous observation [31] (Fig. 5(a)). For the sample M+G−0−5 h (Fig. 5(b)), micron-sized $MnSn(OH)_6$ particles with irregular shapes were found to precipitate on the surfaces of graphene sheets, and these nanoparticles are almost fully amorphous, as confirmed by the XRD diffraction (see Fig. 3(a)). As the temperature increased to 80 °C, the nano-sized $MnSn(OH)_6$ formed at the surface and edge of the graphene sheets, and these nanoparticles display a well crystalline feature with a cubic geometry (Fig. 5(c)), indicating an improved crystallinity. Some of nanoparticles were found to intercalate between the graphene sheets. As the reaction time increased to 24 h, smaller particles and clusters disappeared and homogeneous

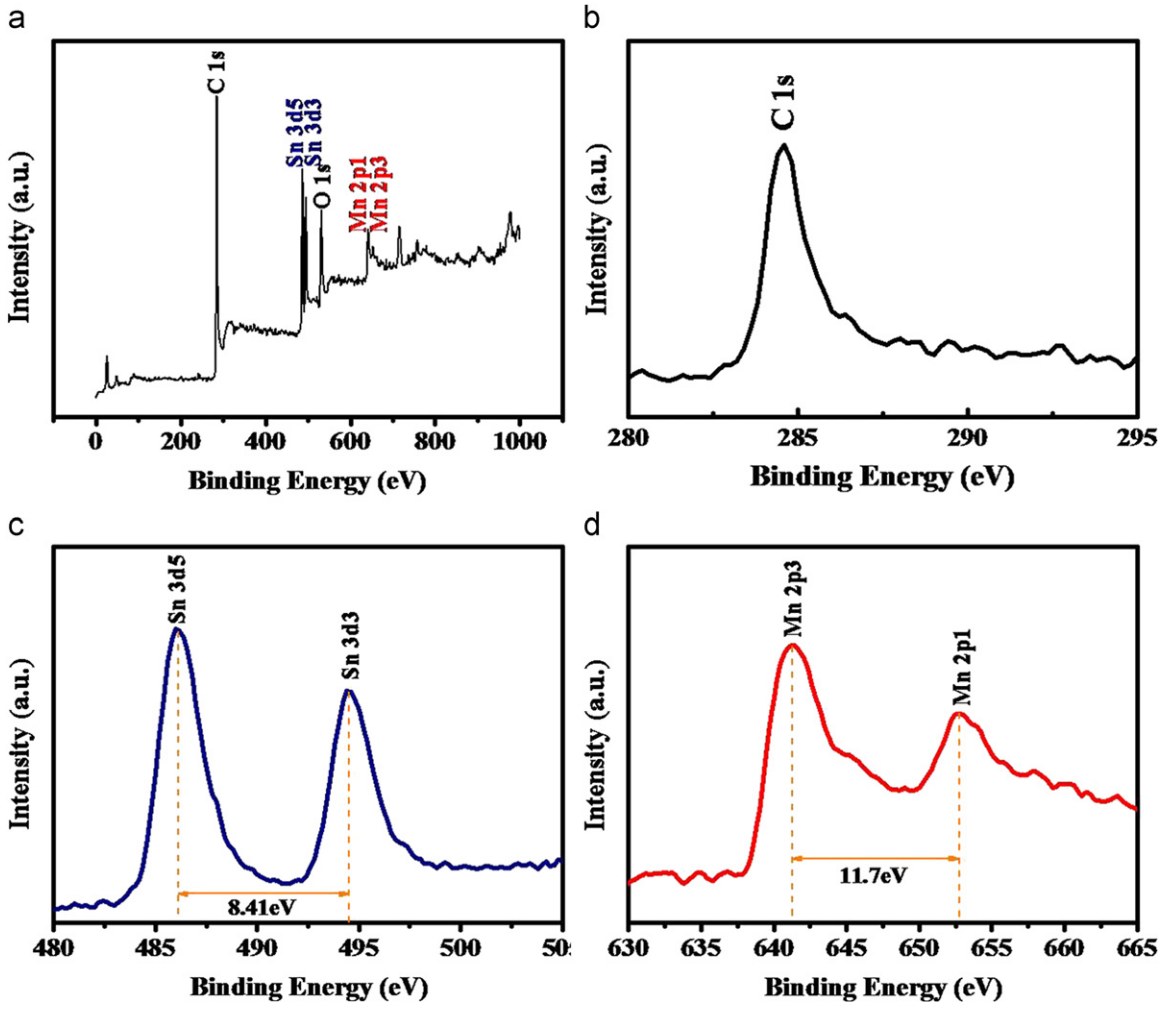

Fig. 4. Surface properties and the valence states of the elements in nanocomposites: (a) large survey, (b) C 1*s* of graphene substrate; Sn 3*d* and Mn 2*p* spectra of the $MnSn(OH)_6$/graphene sample, (c) The Sn 3*d* XPS spectra of the cubic $MnSn(OH)_6$ and (d) the Mn 2*p* XPS spectrum of the cubic $MnSn(OH)_6$.

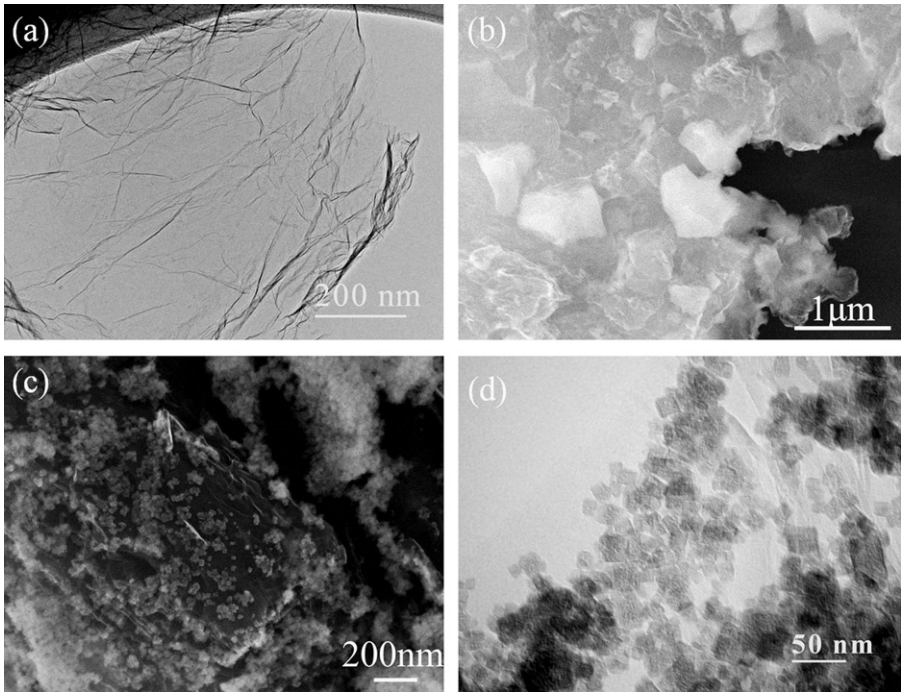

Fig. 5. TEM and SEM images showing the microstructure and morphology of the nanocomposites: (a) TEM image of the graphene sheets, (b) SEM images of M+G−0−5 h, and (c) M+G−80−5 h and (d) TEM image of the M+G−80−24 h.

nanoparticles with the cubic geometry and the size of 20 nm formed on the surfaces of the graphene sheets as shown in Fig. 5(d). The crystal growth occurred upon the Ostwald ripening process as a result of the minimization of the surface tension of individual particles. It is concluded that M+G−80−24 h possessed the highest crystallinity among these samples, consistent with the XRD results (Fig. 3). Both TEM and SEM images confirm that the nanocomposites have no large agglomeration of the $MnSn(OH)_6$ nanoparticles and the entire network still remains porous. The nanocomposites might be promising candidates for capacitor based energy storage applications, where full utilization of the deposited nanoparticles can be realized.

3.2. Electrochemical characterizations

In order to explore the potential applications of $MnSn(OH)_6$/graphene nanocomposites for supercapacitors, the electrochemical properties of the samples M, M+G−0−5 h, M+G−80−5 h and M+G−80−24 h were characterized using CV, galvanostatic charge/discharge and EIS measurements. The average specific capacitance of the electrode can be calculated from the CV curves using the following equation:

$$C = \frac{\int I dt}{m\Delta V} \quad (1)$$

where C is the specific capacitance in F/g, I is the response current, dt is the time differential, m is the mass of electroactive materials and ΔV indicates the voltage range of one sweep segment.

CV curves of the selected samples M, M+G−0−5 h, M+G−80−5 h and M+G−80−24 h were acquired at different scan rates of 5, 10, 20 and 40 mV/s in the potential range of −0.5–0.5 V (vs. SCE) as shown in Fig. 6(a–d). In the case of the sample M, the shape of the CV curves are highly distorted and asymmetric even at the scan rate of 5 mV/s, suggesting the poor charge transfer within the electrodes due to the low electrical conductivity of $MnSn(OH)_6$ nanoparticles. By contrast, the shapes of CV curves for the samples M+G−0−5 h, (b), M+G−80−5 h, (c) and M+G−80−24 h (d) are more symmetric and closer to the rectangle shape, indicating better capacitive behaviors. The better capacitive behaviors can be attributed to the intercalated microstructure in which nano-sized $MnSn(OH)_6$ are well dispersed on a porous graphene network. Moreover, the $MnSn(OH)_6$ nanoparticles may help to prevent the aggregation of graphene sheets providing large amount of conductive diffusion channels and increasing the accessibility of the electrolyte ions.

The relationship between the specific capacitance and the scan rate of the different samples is plotted in Fig. 6(e). The specific capacitance of the sample M was 7.8 F/g at a scan rate of 5 mV/s based on the total mass of the electrode materials, and it decreased to 3.4 F/g at a higher scan rate of 40 mV/s, resulting in about 57% capacitance loss. The specific capacitance of the sample M+G−80−5 h was 18.5 F/g based on total mass of the electrode materials (35.1 F/g based on the mass of $MnSn(OH)_6$) at a scan rate of 5 mV/s, a factor of 2.3 higher than that of the $MnSn(OH)_6$ nanoparticles. At a higher scan rate of 40 mV/s, the specific capacitance decreased to 12.6 F/g based on the total mass of the electrode materials, which is about 32% loss. In contrast, the samples M+G−0−5 h and M+G−80−24 h showed much larger specific capacitance and rate capability, as revealed in the CV measurements. The specific capacitances increased to 31.2 F/g and 32.6 F/g based on the total sample mass at a scan rate of 5 mV/s (59.4 F/g and 62 F/g based on the mass of $MnSn(OH)_6$), respectively. The overall capacitance increased about 300% and 317%, respectively, as compared with that of pure $MnSn(OH)_6$ nanoparticles. The rate-dependent capacity retention maintained with only about 32% and 34% loss as compared with 57% loss in $MnSn(OH)_6$ nanoparticles (based on the total mass of the electrode materials).

The significant improvement in specific capacitance and utilization of the $MnSn(OH)_6$ nanoparticles in the sample M+G−0−5 h is consistent with its almost fully amorphous nature. Specifically, poorly crystallized nano-sized particles may provide larger activated surface areas and defects acting as active sites for redox reactions, meanwhile, shorten the diffusion path of ions from

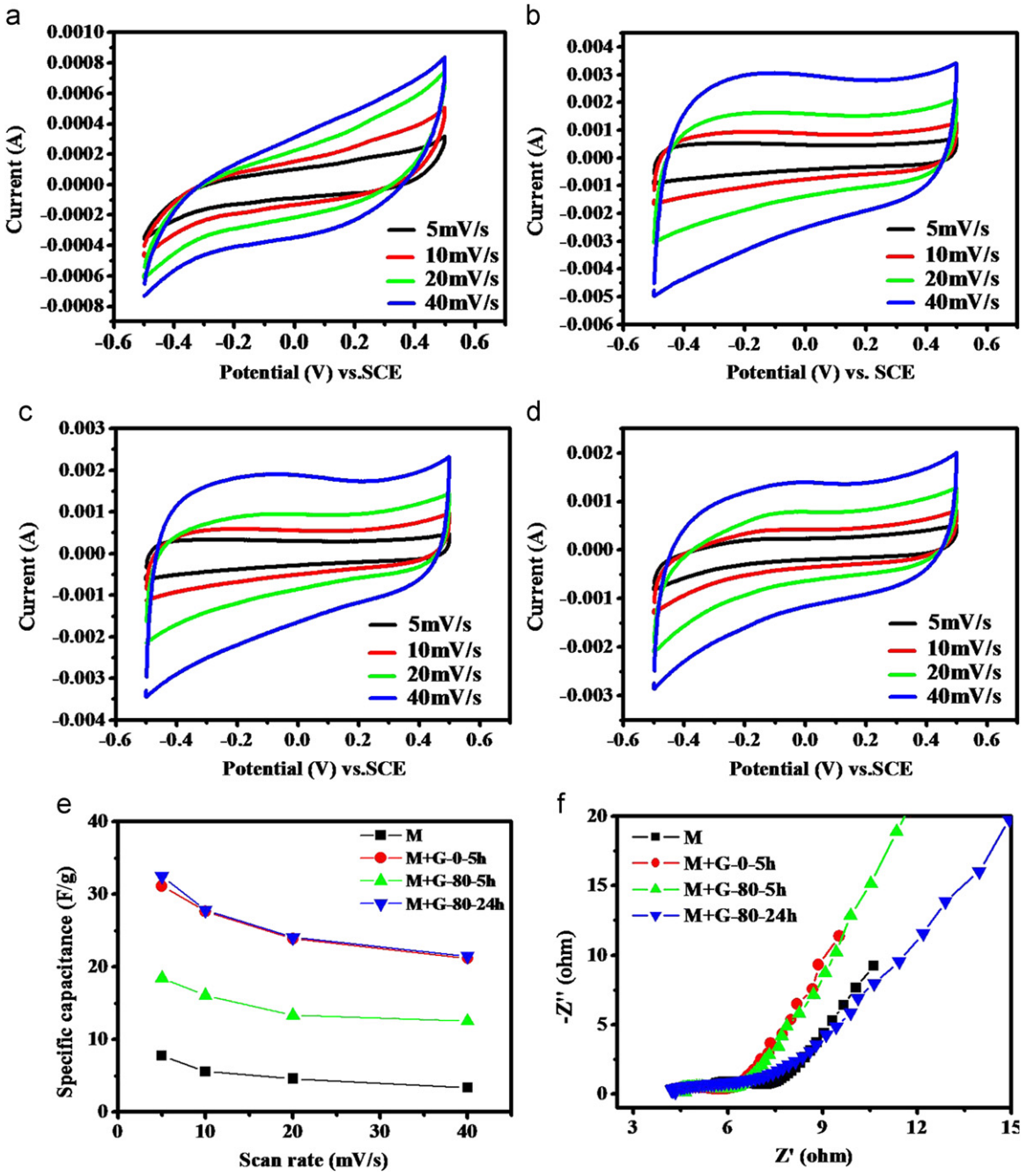

Fig. 6. CV curves of the samples M (a), M+G−0−5 h (b), M+G−80−5 h (c) and M+G−80−24 h (d) at different scan rates of 5, 10, 20 and 40 mV/s in 1 M Na_2SO_4 aqueous solution. (e) Specific capacitance of M, M+G−0−5 h, M+G−80−5 h and M+G−80−24 h at different scan rates of 5, 10, 20 and 40 mV/s in 1M Na_2SO_4 aqueous solution. (f) Nyquist plots of the samples M, M+G−0−5 h, M+G−80−5 h and M+G−80−24 h.

the electrolyte into the electrode [32], resulting a facial access of electrolyte ions into the deeper region of the electrode and thus more stored charges. On the other hand, for the sample M+G−80−24 h, the specific capacitance of 62 F/g (based on the mass of $MnSn(OH)_6$ nanoparticles) is significantly higher than that of the sample M+G−80−5 h (35.2 F/g) as a result of more amount of $MnSn(OH)_6$ nanoparticles formed and deposited on the surfaces of graphene sheets due to the longer co-precipitation reaction time. Therefore, more $MnSn(OH)_6$ nanoparticles connected with graphene sheets in the sample M+G−80−24 h may be utilized during the charge/discharge process than that of sample M+G−80−5 h, contributing to the improvement of the total capacitance.

Complementary to CV measurements, EIS measurements were performed on the selected samples in gaining insights for understanding diffusion characteristics based on the electrochemical frequency behaviors (Fig. 6(f)). Specifically, the Nyquist plot is consisted of a semi-circle at high frequencies and a slope (45° portion of the curve) along the imaginary axis (Z'') at low frequencies, corresponding to charge transfer resistance and Warburg resistance, respectively. The intercept of the semi-circle at a very high frequency represents the equivalent series resistance (ESR) of electrolyte, substrate and contact resistance between the electrode materials and current collectors [33,34]. The ESR of the sample M is significantly greater than the other three, illustrating the poor conductivity of the electrode without the conductive

bridges from the graphene sheets. The slop of the sample M+G−0−5 h is the steepest among the four samples, suggesting the smallest diffusion resistance and best capacitive behavior for the amorphous morphology. The slight slop drop of the M+G−80−5 h may be due to the crystal growth at a higher reaction temperature and the increase of the diffusion resistance. In the case of the sample M+G−80−24 h, the diffusion resistance increases with the larger crystal size and an improved crystallinity for materials synthesized at extended reaction time. Nevertheless, the specific capacitance of the sample M+G−80−24 h is still greater even with larger diffusion resistance than the sample M+G−80−5 h, probably because of more $MnSn(OH)_6$ nanoparticles deposited on the surfaces of graphene sheets with long reaction time. Therefore, the interplay of the defect, crystallinity, particle size and the amount of materials readily for redox reactions affects the ionic transport and charge transfer behaviors and eventually determines the electrochemical performance.

The galvanostatic charge/discharge characteristics were also characterized for the selected sample, e.g., the sample M+G−0−5 h and M are shown in Fig. 7(a and b). For the sample M+G−0−5 h, all the curves at various current densities remain close linearity and symmetry features without obvious IR drops associated with the ESR of the system at the initial stage of discharge. In the case of sample M, the curves do not show the linearity and symmetry features as compared with that of the composite sample, indicating low charge transfer efficiency and large internal resistance of the electrode. The better Faradic efficiency of the composite sample can be attributed to the conductive connection provided by graphene nanosheets between $MnSn(OH)_6$ nanoparticles. There was no obvious capacitance degradation observed over 500 cycles of both sample M+G−0−5 h and M at a current density of 1.5 A/g (Fig. 7(c)). The results indicate that the binary metal hydroxide/graphene nanocomposites possess good charge–discharge properties and excellent electrochemical stability and rate capability used as electrode materials for supercapacitor applications.

4. Conclusions

$MnSn(OH)_6$/graphene nanocomposites were synthesized by a simple co-precipitation method, and the microstructure properties can be tailored by changing the reaction temperature and time. The binary metal hydroxide/graphene displays much improved electrochemical performance (more than 300% improvement) as compared to the monolithic hydroxide nanoparticles alone. The graphene sheets provide a conductive network between the $MnSn(OH)_6$ nanoparticles and current collectors, resulting in the full utilization of the $MnSn(OH)_6$ nanoparticles. The total specific capacitance depends strongly on the crystallinity of the nanoparticles, where the materials with a poor crystallinity showed the maximum specific capacitance of 31.2 F/g (59.4 F/g based on the mass of $MnSn(OH)_6$ nanoparticles) at the scan rate of 5 mV/s. The increase in the specific capacitance for almost fully amorphous materials may be attributed to defects acting as active sites for redox reactions. Furthermore, the EIS measurement indicated that the improved crystallinity and a larger crystal size lead to the increased

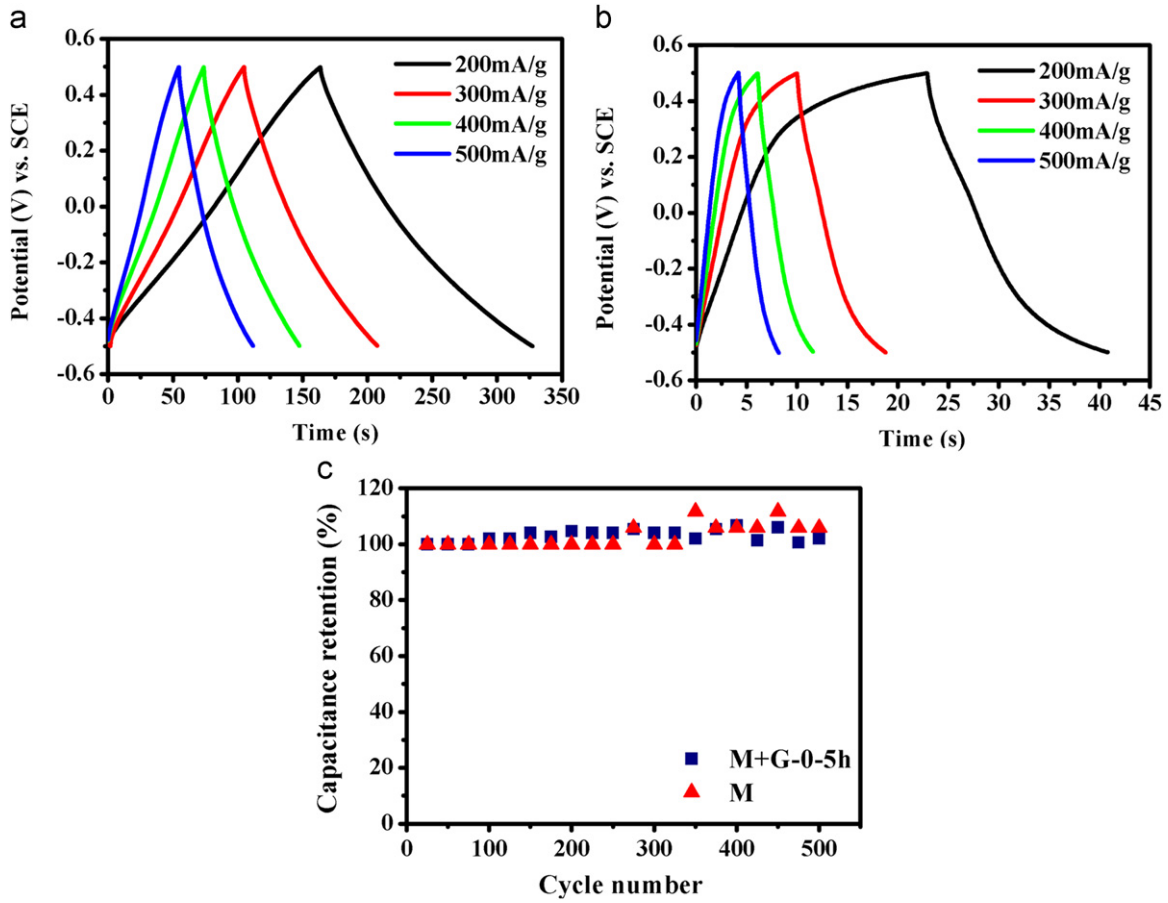

Fig. 7. Galvanostatic charge/discharge curves of the sample (a) M+G−0−5 h and (b) M at different current densities of 200, 300, 400 and 500 mA/g in 1 M Na_2SO_4 aqueous solution. (c) Average specific capacitance retention of the sample M+G−0−5 h and M as a function of the cycle number at a current density of 1.5 A/g in 1 M Na_2SO_4 aqueous solution.

diffusion resistance and thus affect the electrochemical response. The $MnSn(OH)_6$/graphene nanocomposites show a excellent capacity retention without significant degradation after 500 cycles charge/discharge at a current density of 1.5 A/g in 1M Na_2SO_4 aqueous solution. Despite the relatively low specific capacitance, the co-precipitated nanocomposites demonstrate the potential of synergizing conductive graphene nanosheets with pseudo-capacitive materials into one platform for maximizing electrochemical performance. This approach can be applied for synthesizing and designing a wide range of binary metal hydroxide or oxide/graphene nanocomposites for electrochemical energy storage applications.

Acknowledgments

The authors gratefully acknowledge the financial support from the U.S. DOD-Defense Threat Reduction Agency (DTRA) under award HDTRA1-10-1-0002, Graduate Research Innovation Project of Ministry of Education of China (N100602003) and the State Scholarship Fund of China Scholarship Council.

References

[1] M.D. Stoller, S.J. Park, Y.W. Zhu, J.H. An, R.S. Ruoff, Nano Lett. 8 (2008) 3498–3502.
[2] H.L. Wang, H.S. Casalongue, Y.Y. Liang, H.J. Dai, J. Am. Chem. Soc. 132 (2010) 7472–7477.
[3] S. Chen, J.W. Zhu, X.D. Wu, Q.F. Han, X. Wang, ACS Nano 4 (2010) 2822–2830.
[4] A. Rudge, J. Davey, I. Raistrick, S. Gottesfeld, J.P. Ferraris, J. Power Sources 47 (1994) 89–107.
[5] P. Simon, Y. Gogotsi, Nat. Mater. 7 (2008) 845–854.
[6] A.G. Pandolfo, A.F. Hollenkamp, J. Power Sources 157 (2006) 11–27.
[7] A. Burke, J. Power, Sources 91 (2000) 37–50.
[8] R. Kotz, M. Carlen, Electrochim. Acta 45 (2000) 2483–2498.
[9] A. Lewandowski, M. Galinski, J. Power Sources 173 (2007) 822–828.
[10] J. Li, E.H. Liu, W. Li, X.Y. Meng, S.T. Tan, J. Alloys Compd. 478 (2009) 371–374.
[11] L.Z. Fan, Y.S. Hu, J. Maier, P. Adelhelm, B. Smarsly, M. Antonietti, Adv. Funct. Mater. 17 (2007) 3083–3087.
[12] H.F. Li, R.D. Wang, R. Cao, Microporous Mesoporous Mater. 111 (2008) 32–38.
[13] H. Zhang, G.P. Cao, Z.Y. Wang, Y.S. Yang, Z.J. Shi, Z.N. Gu, Nano Lett. 8 (2008) 2664–2668.
[14] C.Z. Meng, C.H. Liu, S.S. Fan, Electrochem. Commun. 11 (2009) 186–189.
[15] J. Yan, T. Wei, B. Shao, F.Q. Ma, Z.J. Fan, M.L. Zhang, C. Zheng, Y.C. Shang, W.Z. Qian, F. Wei, Carbon 48 (2010) 1731–1737.
[16] J. Yan, Z.J. Fan, T. Wei, W.Z. Qian, M.L. Zhang, F. Wei, Carbon 48 (2010) 3825–3833.
[17] J. Yan, T. Wei, B. Shao, Z.J. Fan, W.Z. Qian, M.L. Zhang, F. Wei, Carbon 48 (2010) 487–493.
[18] T.Y. Wei, C.H. Chen, H.C. Chien, S.Y. Lu, C.C. Hu, Adv. Mater. 22 (2010) 347–351.
[19] H. Jena, K.V.G. Kutty, T.R.N. Kutty, Mater. Chem. Phys. 88 (2004) 167–179.
[20] X.L. Fu, X.X. Wang, Z.X. Ding, D.Y.C. Leung, Z.Z. Zhang, J.L. Long, W.X. Zhang, Z.H. Li, X.Z. Fu, Appl. Catal., B 91 (2009) 67–72.
[21] X.L. Fu, D.Y.C. Leung, X.X. Wang, W.W. Xue, X.Z. Fu, Int. J. Hydrogen Energy 36 (2010) 1524–1530.
[22] F. Huang, Z.Y. Yuan, H. Zhan, Y.H. Zhou, J.T. Sun, Mater. Chem. Phys. 83 (2004) 16–22.
[23] S. Zhao, Y. Bai, W.F. Zhang, Electrochim. Acta 55 (2010) 3891–3896.
[24] N. Sharma, K.M. Shaju, G.V.S. Rao, B.V.R. Chowdari, Electrochem. Commun. 4 (2002) 947–952.
[25] W.S. Hummers, R.E. Offeman, J. Am. Chem. Soc. 80 (1958) 1339.
[26] M.J. McAllister, J.L. Li, D.H. Adamson, H.C. Schniepp, A.A. Abdala, J. Liu, M. Herrera-Alonso, D.L. Milius, R. Car, R.K. Prud'homme, I.A. Aksay, Chem. Mater. 19 (2007) 4396–4404.
[27] S. Stankovich, D.A. Dikin, R.D. Piner, K.A. Kohlhaas, A. Kleinhammes, Y. Jia, Y. Wu, S.T. Nguyen, R.S. Ruoff, Carbon 45 (2007) 1558–1565.
[28] D.C. Marcano, D.V. Kosynkin, J.M. Berlin, A. Sinitskii, Z.Z. Sun, A. Slesarev, L.B. Alemany, W. Lu, J.M. Tour, ACS Nano 4 (2010) 4806–4814.
[29] F.H. Li, J.F. Song, H.F. Yang, S.Y. Gan, Q.X. Zhang, D.X. Han, A. Ivaska, L. Niu, Nanotechnology 20 (2009) 455602–455607.
[30] H.W. Nesbitt, D. Banerjee, Am. Miner. 83 (1998) 305–315.
[31] W. Lv, D.M. Tang, Y.B. He, C.H. You, Z.Q. Shi, X.C. Chen, C.M. Chen, P.X. Hou, C. Liu, Q.H. Yang, ACS Nano 3 (2009) 3730–3736.
[32] J.K. Chang, Y.L. Chen, W.T. Tsai, J. Power Sources 135 (2004) 344–353.
[33] T. Zhao, H. Jiang, J. Ma, J. Power Sources 196 (2011) 860–864.
[34] J. Yan, T. Wei, W.M. Qiao, B. Shao, Q.K. Zhao, L.J. Zhang, Z.J. Fan, Electrochim. Acta 55 (2010) 6973–6978.